

Computational modeling of electrocardiograms: A finite element approach toward cardiac excitation

M. Kotikanyadanam, S. Göktepe and E. Kuhl^{*,†}

Departments of Mechanical Engineering and Bioengineering, Stanford University, Stanford, CA 94305, U.S.A.

SUMMARY

The objective of this work is the computational simulation of a patient-specific electrocardiogram (EKG) using a novel, robust, efficient, and modular finite element-based simulation tool for cardiac electrophysiology. We apply a two-variable approach in terms of a fast action potential and a slow recovery variable, whereby the latter phenomenologically summarizes the concentration of ionic currents. The underlying algorithm is based on a staggered solution scheme in which the action potential is introduced globally as nodal degree of freedom, while the recovery variable is treated locally as internal variable on the integration point level. We introduce an unconditionally stable implicit backward Euler scheme to integrate the evolution equations for both variables in time, and an incremental iterative Newton–Raphson scheme to solve the resulting nonlinear system of equations. In a straightforward post-processing step, we calculate the flux of the action potential and integrate it over the entire domain to obtain the heart vector. The projection of the heart vector onto six pre-defined directions in space defines a six-lead EKG. We illustrate its generation in terms of a magnetic resonance-based patient-specific heart geometry and discuss the clinical implications of the computational electrocardiography. Copyright © 2009 John Wiley & Sons, Ltd.

Received 2 March 2009; Accepted 16 April 2009

KEY WORDS: finite element method; biomechanics; electrophysiology; excitation; Aliev–Panfilov model; electrocardiogram

1. MOTIVATION

Heart disease is the leading cause of death and disability in both industrialized nations and the developing world, accounting for approximately 40% of all human mortality. Almost 80 million Americans, one in three, have one or more types of cardiovascular disease, generating an annual health care cost in excess of \$430 billion [1]. Without early diagnosis and appropriate treatment, cardiac disease can have devastating physiological consequences. For more than a century, the electrocardiogram (EKG) has served as a crucial diagnostic tool that monitors the electrical activity of the heart to identify rhythm disturbances, changes in electrical conduction, myocardial ischemia, and myocardial infarction [2, 3].

On the microscopic level, electrical activity is coordinated by time-varying electrical and chemical gradients across the cell membrane. These gradients are caused by the complex interaction of different ion channels controlling the inward and outward flux of charged sodium, potassium,

*Correspondence to: E. Kuhl, Departments of Mechanical Engineering and Bioengineering, Stanford University, Stanford, CA 94305, U.S.A.

†E-mail: ekuhl@stanford.edu

and calcium ions [4, 5]. More than half a century ago, Hodgkin and Huxley [6] presented the first quantitative model for membrane currents in an excitable nerve cell that constitutes the basis for most cardiac cell models today [7–10]. The classical Hodgkin–Huxley model was simplified significantly by FitzHugh [11] and Nagumo *et al.* [12] who introduced an extremely elegant two-variable formulation that allows for a rigorous mathematical analysis with well-established analytical tools. The FitzHugh–Nagumo model is characterized through a fast action potential ϕ , and a slow recovery variable r . The latter summarizes the effects of all ionic currents in one single phenomenological variable [13]. In what follows, we apply a slightly modified version, the two-variable Aliev–Panfilov model [14], which is particularly tailored to model the fast upstroke and the extended action potential plateau of ventricular cardiomyocytes. To date, the Aliev–Panfilov model has primarily been solved with three-dimensional explicit finite difference solution schemes [15–18], or with two-dimensional finite element schemes on the cardiac surface [19, 20]. In the view of a potential monolithic coupling of excitation and contraction, we introduce a modular implicit integration scheme to solve the spatio-temporal Aliev–Panfilov equations within a fully three-dimensional finite element approach [21, 22]. In this manuscript, we seek to apply this algorithm to better understand cardiac excitation patterns in real patient-specific geometries.

On the macroscopic level, rhythmic cardiac contraction is coordinated through nonlinear electrical waves of excitation which propagate smoothly through the cardiac tissue. A global quantity that summarizes the electric activity of the heart is the heart vector generated by integrating all local wave propagation vectors over the cardiac domain. The time-varying projection of the heart vector onto particular directions is called the electrocardiogram, or short EKG, [23, 24]. Figure 1 shows a generic EKG segment consisting of a small, slow hump called the P wave, a sharp dip-rise-dip segment called the QRS complex, and a small, slow hump called the T wave [4, 25]. These features, in essence variations in potential differences, correspond to different events in the cardiac cycle. The P wave is caused by the depolarization of the atria. The atria then contract and empty the blood into the ventricles. The QRS complex is caused by the depolarization of the ventricles. This is the phase when the ventricles contract and pump blood out. Finally, the T wave is caused by the repolarization of the ventricles. Abnormalities in any of these cardiac events change the corresponding segment in the EKG. The EKG thus provides a valuable diagnostic tool to monitor diseases of the heart in a simple, noninvasive way.

The central goal of this manuscript is to design a generic algorithm that can generate EKGs based on patient-specific cardiac geometries. In Section 2 we briefly summarize the governing equations of cardiac excitation in their two-variable Aliev–Panfilov form. Section 3 illustrates both their temporal and spatial discretizations, and the consistent linearization of the underlying system

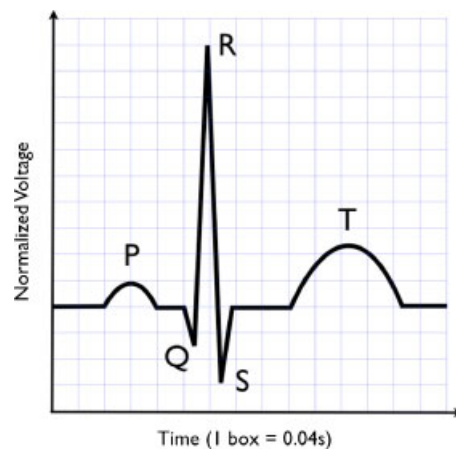


Figure 1. Generic electrocardiogram with characteristic P wave monitoring the depolarization of the atria, QRS complex indicating the depolarization of the ventricles, and T wave monitoring the repolarization of the ventricles.

of equations. In Section 4, we demonstrate the computational generation of an EKG based on a patient-specific magnetic resonance image. In Section 5, we close by discussing the limitations of our computational tool set, and illustrate its clinical potential as a diagnostic tool to identify and interpret cardiac arrhythmias.

2. CONTINUOUS PROBLEM OF CARDIAC EXCITATION

The excitation of cardiac tissue can be modeled through a coupled system of equations for the cardiac action potential ϕ and a set of variables that characterize the effects of charged sodium, potassium, and calcium currents. In the simplest case, these ionic effects can be lumped into one single phenomenological variable r , which is referred to as recovery variable. In this section, we briefly summarize the equations for the fast action potential and the slow recovery variable based on the generalized FitzHugh–Nagumo equations [11, 12] in their refined Aliev–Panfilov version [14, 21]. To account for the propagating nature of excitation waves, a phenomenological flux term is introduced for the action potential ϕ , while the recovery variable r is assumed to be strictly local.

2.1. The excitation problem

The excitation problem is characterized through the spatio-temporal evolution of the action potential ϕ in terms of the flux, $\text{div } \mathbf{q}$, and the source term, f^ϕ

$$\dot{\phi} = \text{div } \mathbf{q}(\phi) + f^\phi(\phi, r) \quad (1)$$

It has become common practice to enhance the strictly local FitzHugh–Nagumo equations by a phenomenological action potential flux $\text{div } \mathbf{q}$ with

$$\mathbf{q} = \mathbf{D} \cdot \nabla \phi \quad (2)$$

to account for the nonlocal propagating nature of excitation waves. Action potential propagation is characterized through the second-order diffusion tensor $\mathbf{D} = d^{\text{iso}} \mathbf{I} + d^{\text{ani}} \mathbf{n} \otimes \mathbf{n}$ which can account for both isotropic propagation d^{iso} and anisotropic propagation d^{ani} along a preferred direction \mathbf{n} . The source term f^ϕ

$$f^\phi = c\phi[\phi - \alpha][1 - \phi] - r\phi \quad (3)$$

consists of a cubic polynomial in terms of the action potential $c\phi[\phi - \alpha][1 - \phi]$, and a coupling term introducing the recovery variable r . The parameter α is referred to as oscillation threshold. Cardiac muscle cells typically display a stable action potential with positive α values.

2.2. The recovery problem

While it is common to assume a spatial propagation of the action potential, the evolution equation for the recovery variable is usually assumed to be strictly local

$$\dot{r} = f^r(\phi, r) \quad (4)$$

governed solely through the source term f^r

$$f^r = [\gamma + r\bar{\gamma}(\phi)][-r - c\phi[\phi - b - 1]] \quad (5)$$

In contrast to the traditional FitzHugh–Nagumo model, the additional weighting factor $[\gamma + r\bar{\gamma}(\phi)]$ with $\bar{\gamma}(\phi) = \mu_1/[\mu_2 + \phi]$ has been introduced by Aliev and Panfilov [14] to phenomenologically tune the restitution curve through the parameters μ_1 and μ_2 . The system of Equations (1) and (4) represents the classical FitzHugh–Nagumo equations [11, 12] for the particular choice of $f^\phi = c[\phi[\phi - \alpha][1 - \phi] - r]$ and $f^r = \phi - br + a$.

3. DISCRETE PROBLEM OF CARDIAC EXCITATION

We suggest to discretize the coupled spatio-temporal excitation equations (1) and (4) with a finite difference scheme in time and a finite element scheme in space. Owing to the global nature of the action potential introduced through the diffusion term $\text{div} \mathbf{q}(\phi)$, we propose a \mathcal{C}^0 -continuous finite element interpolation for the action potential ϕ , while a \mathcal{C}^{-1} -continuous interpolation is sufficient for the recovery variable r . Accordingly, we introduce the action potential as a global degree of freedom on each finite element node, whereas the recovery variable is introduced locally on the integration point level. The resulting staggered system is solved with an incremental iterative Newton–Raphson solution procedure based on the consistent linearization of the discrete excitation problem [21, 22].

3.1. The excitation problem

We begin by transforming the nonlinear excitation equation (1) into its residual form $\mathbf{R}^\phi = \dot{\phi} - \text{div}(\mathbf{q}) - f^\phi \doteq 0$ in \mathcal{B}_ϕ , which we complement by the corresponding Dirichlet and Neumann boundary conditions $\phi = \bar{\phi}$ on $\partial\mathcal{B}_\phi$ and $\mathbf{q} \cdot \mathbf{n} = \bar{q}$ on $\partial\mathcal{B}_q$. For most physiologically relevant excitation problems, homogeneous Neumann boundary conditions $\mathbf{q} \cdot \mathbf{n} = 0$ are applied on the entire boundary $\partial\mathcal{B}$. The weak form of the excitation residual is obtained by an integration over the domain \mathcal{B} , the standard integration by parts, and the inclusion of the Neumann boundary conditions. For its spatial discretization, we discretize the domain of interest \mathcal{B} with n_{el} finite elements \mathcal{B}_e as $\mathcal{B} = \bigcup_{e=1}^{n_{\text{el}}} \mathcal{B}_e$ and apply the standard isoparametric concept to interpolate the trial functions ϕ^h and the test functions $\delta\phi^h$.

$$\delta\phi^h|_{\mathcal{B}^e} = \sum_{i=1}^{n_{\text{el}}} N^i \delta\phi_i \quad \text{and} \quad \phi^h|_{\mathcal{B}^e} = \sum_{j=1}^{n_{\text{el}}} N^j \phi_j \tag{6}$$

Here, N are the standard shape functions on the element level and $i, j = 1, \dots, n_{\text{el}}$ are the n_{el} element nodes. For the temporal discretization, we partition the time interval of interest \mathcal{T} into n_{stp} subintervals $[t_n, t_{n+1}]$ as $\mathcal{T} = \bigcup_{n=0}^{n_{\text{stp}}} -1[t_n, t_{n+1}]$ and apply a standard backward Euler time integration scheme in combination with a finite difference approximation of the first-order time derivative $\dot{\phi}$.

$$\dot{\phi} = [\phi - \phi_n] / \Delta t \tag{7}$$

Herein, the index $(\circ)_{n+1}$ has been omitted for the sake of clarity, and the common abbreviation $\Delta t := t - t_n > 0$ has been introduced for current time increment. With the discretizations in space (6) and time (7), the discrete algorithmic residual \mathbf{R}_I^ϕ takes the following explicit representation:

$$\mathbf{R}_I^\phi = \mathbf{A} \int_{e=1}^{n_{\text{el}}} N^i \frac{\phi - \phi_n}{\Delta t} + \nabla N^i \cdot \mathbf{q} \, dV - \int_{\partial\mathcal{B}_q^e} N^i \bar{q} \, dA - \int_{\mathcal{B}^e} N^i f^\phi \, dV \doteq 0 \tag{8}$$

The operator \mathbf{A} symbolizes the assembly of all element contributions at the element nodes $i = 1, \dots, n_{\text{el}}$ to the overall residual at the global node points $I = 1, \dots, n_{\text{nd}}$. To solve the discrete system of nonlinear equations (8), we suggest an incremental iterative Newton–Raphson solution technique based on the consistent linearization of the residual which introduces the global iteration matrix \mathbf{K}_{IJ}^ϕ .

$$\mathbf{K}_{IJ}^\phi = \partial_{\phi_j} \mathbf{R}_I^\phi = \mathbf{A} \int_{e=1}^{n_{\text{el}}} N^i \frac{1}{\Delta t} N^j + \nabla N^i \cdot \mathbf{D} \cdot \nabla N^j - N^i d_\phi f^\phi N^j \, dV \tag{9}$$

For each incremental iteration, we update the global vector of unknowns $\phi_I \leftarrow \phi_I - \sum_{J=1}^{n_{\text{nd}}} \mathbf{K}_{IJ}^{\phi-1} \mathbf{R}_J^\phi$ at all global $I = 1, \dots, n_{\text{nd}}$ global nodes. In the following subsection, we illustrate the iterative calculation of the source term $f^\phi(\phi, r)$ and its consistent algorithmic linearization $d_\phi f^\phi(\phi, r)$ required to evaluate the global residual (8) and the global iteration matrix (9).

3.2. The recovery problem

The recovery variable r is introduced as an internal variable and stored locally on the integration point level. For its temporal discretization, we apply a finite difference approximation

$$\dot{r} = [r - r_n] / \Delta t \quad (10)$$

combined with a classical implicit Euler backward time integration scheme. Accordingly, the discrete residual statement of the recovery Equation (4) takes the following format:

$$\mathbf{R}^r = r - r_n - [[\gamma + r\bar{\gamma}][r - c\phi[\phi - b - 1]]]\Delta t \doteq 0 \quad (11)$$

Its consistent linearization

$$\mathbf{K}^r = \partial_r \mathbf{R}^r = 1 + [\gamma + \bar{\gamma}[2r + c\phi[\phi - b - 1]]]\Delta t \quad (12)$$

defines the iteration scheme for the incremental update of the recovery variable $r \leftarrow r - \mathbf{K}^{r-1} \mathbf{R}^r$ on the integration point level. At equilibrium, we finally compute the source term for $f^\phi = c\phi[\phi - \alpha][1 - \phi] - r\phi$ the excitation problem (8) and its linearization $d_\phi f^\phi = \partial_\phi f^\phi + \partial_r f^\phi d_\phi r$ for the global Newton iteration (9). The latter takes the following explicit representation: $d_\phi f^\phi = c[-3\phi^2 + 2[1 + \alpha]\phi - \alpha] - r - \phi d_\phi r$. The sensitivity of the recovery variable $d_\phi r$ with respect to the action potential ϕ is determined at local equilibrium $d_\phi \mathbf{R}^r = \partial_\phi \mathbf{R}^r + \partial_r \mathbf{R}^r d_\phi r \doteq 0$ as $d_\phi r = -[\mathbf{K}^r]^{-1} \partial_\phi \mathbf{R}^r$. Herein, \mathbf{K}^r is the tangent (12) at local equilibrium, and the partial derivative is determined from the local residual (11) as $\partial_\phi \mathbf{R}^r = [[\gamma + r\bar{\gamma}]c[2\phi - b - 1] - r\partial_\phi \bar{\gamma}[r + c\phi[\phi - b - 1]]]\Delta t$ with $\partial_\phi \bar{\gamma} = \mu_1 / [\mu_2 + \phi]^2$.

4. EXAMPLE OF CARDIAC EXCITATION

In this section, we apply the proposed algorithm to calculate the excitation in a patient-specific heart geometry generated from magnetic resonance imaging. Magnetic resonance imaging produces a sequence of two-dimensional images captured at different depths as shown in Figure 2, left. Cardiac tissue is then identified manually and isolated using standard image processing techniques. A simple thresholding and binary masking operation convert the noisy, grayscale images to monochrome images with sharply defined boundaries. A preliminary triangular surface mesh is formed from these slices, and is then converted to a volume mesh as displayed in Figure 2, right. The generated finite element mesh shown in Figure 2 has 3129 nodes and 11 347 three-dimensional tetrahedral muscle elements. In order to include a fast conduction system of Purkinje fibers, we manually inserted 112 two-dimensional line elements sharing the muscle element nodes but having a higher conductivity. Known activation times of various regions of the heart were used as the validation checks to guide the distribution of these fast conduction elements. Guided by the literature [26], the conductivity of the ventricular muscle tissue is assumed to be isotropic $\mathbf{D} = d\mathbf{I}$, with $d = 10 \text{ mm}^2/\text{ms}$. The conductivity of the Purkinje fibers is assumed to be twenty times higher, i.e. $d = 200 \text{ mm}^2/\text{ms}$.

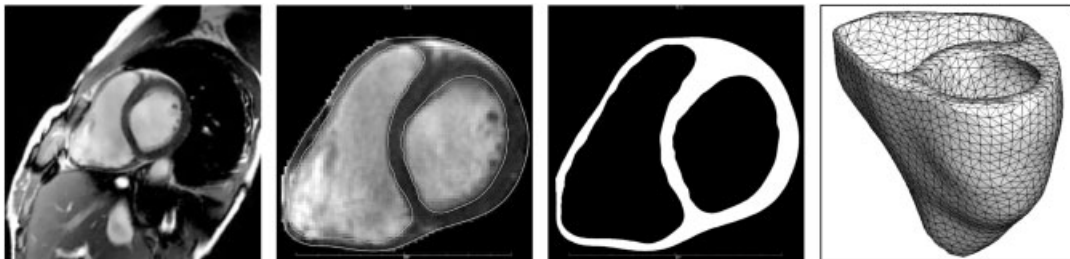


Figure 2. Generation of a human heart model: Magnetic resonance image, segmentation, binary mask of one particular cross section, and finite element mesh, from left to right.

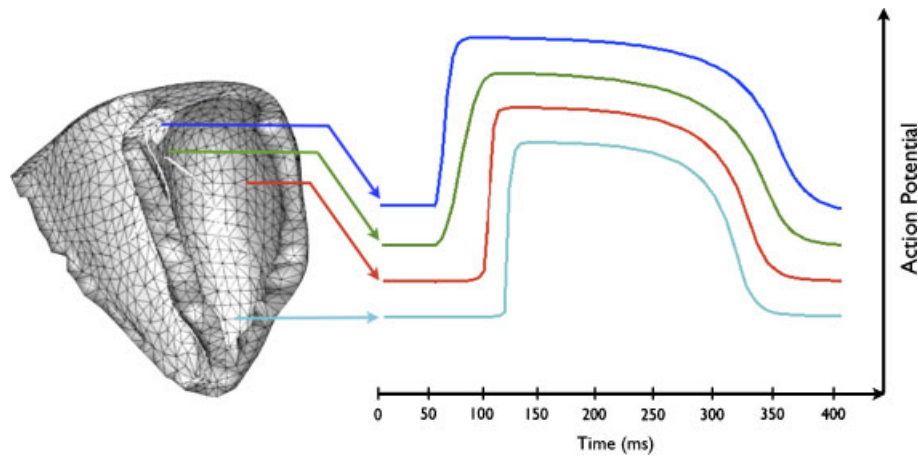


Figure 3. Typical transmembrane action potentials for different regions of the heart. Basal regions of the septum are depolarized first, display the longest action potential duration, and are repolarized last. To account for different plateau length in the model, the action potential duration is scaled with the activation time.

An important characteristic of cardiac cells is their individual action potential duration. In the real heart, the action potential duration of cells in the endocardium is almost twice as large as the action potential duration of epicardial cells. This implies that the first cells to depolarize will be the last ones to repolarize [26]. From the point of view of pumping, this means that the endocardium, and especially the septum, acts as an anchor which the outer lying muscle cells wring around. We assume the action potential duration at any given point to be linearly interpolated between a limiting action potential durations, the interpolant being the activation time t^{act} . For our excitation formulation this implies that the non-dimensional Aliev–Panfilov equations (1) and (4) are scaled through

$$\Phi = [100\phi - 80,] \text{ mV} \quad \text{and} \quad \tau = 12.9 \left[1 - \tau_0 \frac{t^{act} - t_0}{t_1 - t_0} \right] t \text{ ms}$$

to obtain the physiological action potential amplitude Φ ranging from -80 mV to $+20$ mV and the characteristic activation-time-dependent action potential durations τ . Here, we suggest $\tau_0 = 0.45$, $t_1 = 94$ ms, and $t_0 = 12$ ms. This means that the later a region activates, the shorter the action potential duration of that region, as illustrated in Figure 3. The remaining Aliev–Panfilov parameters are chosen as $\alpha = 0.05$, $\gamma = 0.002$, $b = 0.15$, and $c = 8$. As initial conditions, all ventricular nodes are assigned as a resting action potential value of $\Phi = -80$ mV. Moreover, we assume homogeneous Neumann boundary conditions for the entire structure, i.e. the entire cardiac surface is assumed to be flux free, $\mathbf{q} \cdot \mathbf{n} = 0$. The chosen time-step size is $\Delta t = 1$ ms.

4.1. Cardiac activation

Figure 4 shows a time series capture of the cardiac electrophysical cycle. At rest, the transmembrane potential of all cardiac cells is approximately -80 mV. Depolarization first begins at the atrioventricular node that acts as electrical pacemaker stimulating its neighboring cells to generate a depolarization across their cell membrane, see [27]. Once this depolarization exceeds a threshold of about -50 mV, the transmembrane potential increases rapidly from the resting state of -80 mV to the excited state of approximately $+20$ mV. The Purkinje fibers, shown in yellow, rapidly conduct the action potential from the base of the septum down to the apex. The myocytes themselves also conduct the signal, albeit much slower. Depolarization proceeds as a wave, and eventually the entire heart is depolarized at $t = 0.15$ s. There is then a short pause of about 0.1 s, during which the heart remains depolarized at $+20$ mV. Repolarization first begins at the lateral epicardium and proceeds roughly in the opposite sequence as depolarization. The last cells to

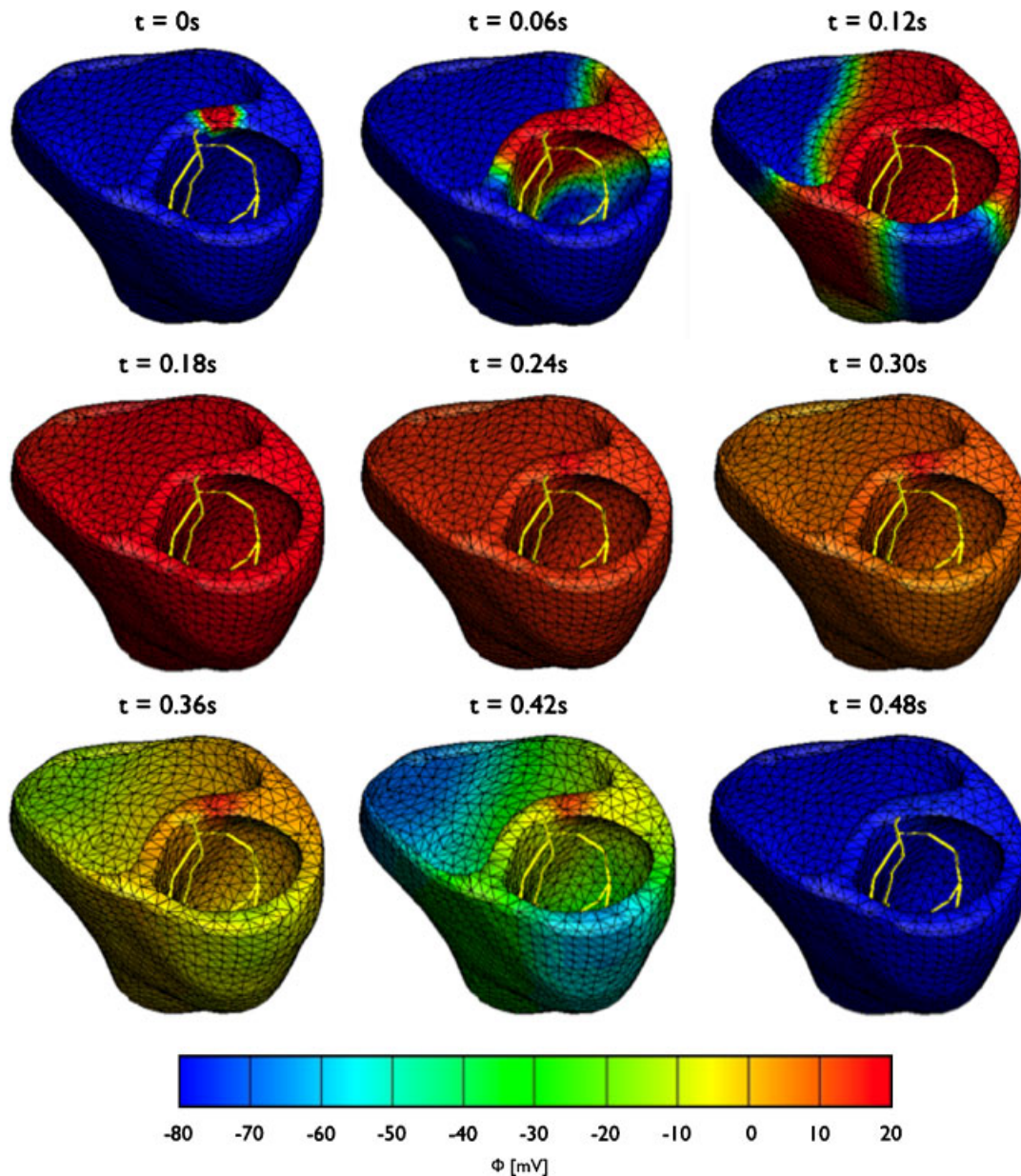


Figure 4. Sequence of excitation of a patient-specific human heart. Depolarization begins at the base of the septum and is rapidly conducted down to the apex through the Purkinje fibers, shown in yellow. After a plateau of complete depolarization, the heart repolarizes in reverse order.

depolarize are the first ones to repolarize. Approximately at $t = 0.5$ s, the entire heart is repolarized at -80 mV, and the cardiac cycle is complete.

4.2. Computation of heart vector and EKG

In the following subsection, we will calculate the heart vector and a corresponding six-lead EKG for the patient-specific excitation model discussed in the previous subsection. When a six-lead EKG is taken, three electrodes called the limb leads are placed below the right and left collarbones and on the left thigh. Potential differences are measured between every two leads, and between each lead and the mean of all three leads, giving a total of six time-varying potential differences.

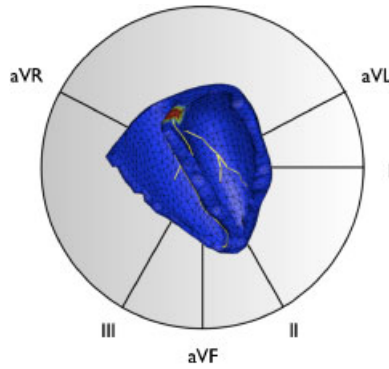


Figure 5. Orientation of measurement axes for a six-lead EKG. Lead I measures the potential difference between the right and left arm, lead II between the right arm and the left leg, and lead III between the left arm and the left leg. The augmented limb lead aVR is the related to the right arm, aVL is related to the left arm, and aVF is related to the left leg.

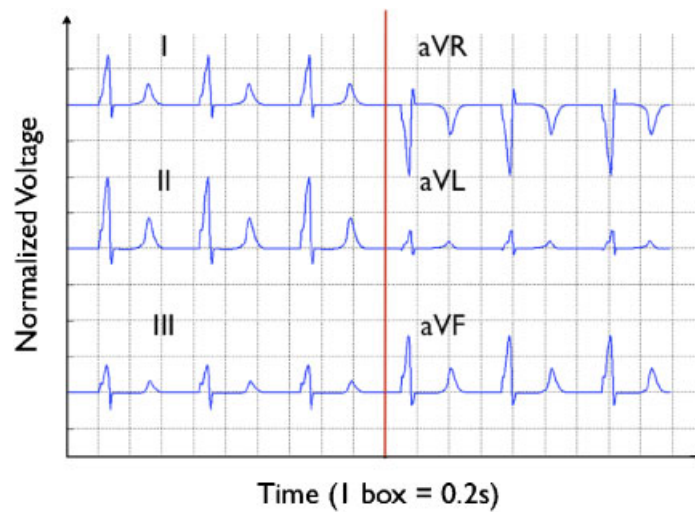


Figure 6. Computationally simulated patient-specific six-lead EKG. Virtual recordings are generated by projecting the heart vector onto the six leads. Recordings display the characteristic QRS complex associated with the depolarization of the ventricles and the T wave monitoring their repolarization.

These can be viewed as the projections of the heart vector onto six different measurement vectors [28] as shown in the Figure 5. In our work, we model the heart vector $\mathbf{q}^{\text{heart}}$ as the integrated sum of the electric flux \mathbf{q} at all points in the heart. Since we apply an implicit finite element scheme, the heart vector

$$\mathbf{q}^{\text{heart}} = \int_{\mathcal{B}} \mathbf{q} dV \quad \text{with } \mathbf{q} = \mathbf{D} \cdot \nabla \phi$$

is readily available at equilibrium through a straightforward post-processing step in which we calculate the potential flux \mathbf{q} and integrate it numerically over the entire heart. We chose the lead II vector to point from the base of the septum to the apex, and the aVL vector to be perpendicular to it, cutting across the ventricles. Since all six vectors lie in one plane, only two of them are linearly independent.

Projected on this configuration of measurement vectors, the heart vector $\mathbf{q}^{\text{heart}}$ generates the EKG illustrated in Figure 6. Consider the sequence of cardiac events as seen by lead II, starting from the point in time when the ventricles are fully relaxed. The initial depolarization wavefront

proceeds from the base of the septum to the apex very rapidly, making the component of the heart vector along lead II to rise rapidly. This is the so-called R wave in the EKG. After the wave reaches the apex, it goes back to the heart via the ventricular walls, and this causes the lead II component to quickly fall below zero, forming the S wave. When the ventricles are completely depolarized, there is no wavefront and hence no signal recorded. After a brief pause which, in the real heart, allows the ventricles to fully empty out the blood, a wave of repolarization starts from the outer ventricular muscles and proceeds back to the base of the septum. This backward-propagating repolarization wave again causes the lead II component of the heart vector to slowly increase, forming the T wave. Finally, when the entire heart has repolarized, there are no more wavefronts and the EKG returns to its baseline voltage known as the isoelectric line. At this point, in a real heart, the atrial depolarization causes a similar rise and fall in the potential, the P wave, and the sequence of events described repeats itself. We do not model the atria, and hence our EKGs do not contain the P wave. However, the main characteristics of the EKG, such as ST interval, polarity of the R and T waves, presence of biphasic waves, and relative amplitudes of R and T waves match well with typical real EKGs. The shape of the T wave of the EKG is extremely sensitive to the distribution of the action potential duration. With a homogeneous action potential duration for $\tau_0=0$, the model would predict an inverted T wave. As a matter of fact, there is a range of diseases related to action potential duration distributions that can be diagnosed by the shape of the T wave.

5. DISCUSSION

In this manuscript, we have presented our first attempts to model cardiac excitation in real anatomic heart geometries. We have validated our algorithm in terms of a computationally generated EKG. In contrast to the most existing computational schemes, our approach is not based on explicit finite differences, but on implicit finite element techniques. Accordingly, we can utilize relatively coarse temporal and spatial discretizations, while still being capable to resolve sharp depolarizing wave fronts and repolarizing wave tails. It is the use of implicit time integration schemes that render our method extremely robust. The particular finite element discretization with just one global degree of freedom per node paired with a quadratically converging Newton–Raphson solution procedure has proven to be very efficient. Real heart excitation problems can be run on virtually any laptop or desktop computer to reproduce EKGs that are in surprisingly good agreement with clinical observations. Our algorithm thus has tremendous potential to complement clinical EKG recordings for quick and accurate diagnosis.

A typical example is acute myocardial infarction associated with the partial or total occlusion of a major coronary artery. Owing to the lack of blood supply, cardiac muscle tissue in the affected region soon begins to die. The successful treatment of acute myocardial infarction crucially relies on a rapid and precise localization of the infarcted region to instantaneously restore blood supply. In the EKG recording, damaged cardiac tissue manifests itself in abnormal ST segments in the leads sampling the area of the heart that is supplied by the occluded artery. Cardiologists are trained to interpret abnormal EKGs for generic cardiac geometries assuming an average generic baseline pattern. In reality, however, every heart is different in dimension and mass, and the generic interpretation might not apply for the individual patient under consideration. Eventually, the presented computational tool can be embedded in a real-time patient-specific inverse analysis, aiming to reconstruct damaged areas of the heart for a given recorded EKG and a given measured patient-specific cardiac geometry. The three-dimensional virtual assessment of excitation patterns displayed on the patient's own heart will ultimately enable the precise identification of the affected area, and significantly improve the therapeutic treatment on an individual basis. The quantitative validation of our EKG simulation tool for healthy and diseased hearts forms an integral part of our current research activities. In the future, we aim at coupling the finite element-based electrical excitation algorithm to the mechanical contraction problem in a unique monolithic way to further explore how rhythm disturbances affect cardiac muscle contraction and the generation of cardiac output.

ACKNOWLEDGEMENTS

This material is based on work supported by the National Science Foundation under Grant No. EFRI-CBE 0735551 Engineering of cardiovascular cellular interfaces and tissue constructs. We thank Dr Euan Ashley for providing the patient-specific magnetic resonance image, and Anton Dam, Rebecca Taylor, and Daniel Burkhart for their valuable help in meshing the data.

REFERENCES

1. Rosamond W, Flegal K, Friday G, Furie K, Go A, Greenlund K, Haase N, Ho M, Howard V, Kissela B, Kittner S, Lloyd-Jones D, McDermott M, Meigs J, Moy C, Nichol G, O'Donnell C, Roger V, Rumsfeld J, Sorlie P, Steinberger J, Thom T, Wasserthiel-Smoller S, Hong Y. Heart disease and stroke statistics—2007 update: a report from the American Heart Association Statistics Committee and Stroke Statistics Subcommittee. *Circulation* 2007; **115**:69–171.
2. Braunwald E. *Heart Disease: A Textbook of Cardiovascular Medicine*. Saunders Co: Philadelphia, 1997.
3. Einthoven W. The different forms of the human electrocardiogram and their signification. *Lancet* 1912; **1**:853–861.
4. Berne RM, Levy MN. *Cardiovascular Physiology*. The Mosby Monograph Series. Mosby: St. Louis, 2001.
5. Opie LH. *Heart Physiology: From Cell to Circulation*. Lippincott Williams & Wilkins: Philadelphia, 2003.
6. Hodgkin AL, Huxley AF. A quantitative description of membrane current and its application to conductance and excitation in nerve. *Journal of Physiology* 1952; **117**:500–544.
7. Beeler GW, Reuter H. Reconstruction of the action potential of ventricular myocardial fibers. *Journal of Physiology* 1977; **268**:177–210.
8. Clayton RH, Panfilov AV. A guide to modelling cardiac electrical activity in anatomically detailed ventricles. *Progress in Biophysics and Molecular Biology* 2008; **96**:19–43.
9. Luo C, Rudy Y. A model of the ventricular cardiac action potential. Depolarization, repolarization, and their changes. *Circulation Research* 1991; **68**:1501–1526.
10. Noble D. A modification of the Hodgkin–Huxley equations applicable to Purkinje fibre action and pacemaker potentials. *Journal of Physiology* 1962; **160**:317–352.
11. FitzHugh R. Impulses and physiological states in theoretical models of nerve membranes. *Biophysical Journal* 1961; **1**:445–466.
12. Nagumo J, Arimoto S, Yoshizawa S. Active pulse transmission line simulating nerve axon. *Proceedings of the Institute of Radio Engineers* 1962; **50**:2061–2070.
13. Keener J, Sneyd J. *Mathematical Physiology*. Springer Science and Business Media. Springer: Berlin, 2004.
14. Aliev RR, Panfilov AV. A simple two-variable model of cardiac excitation. *Chaos, Solitons and Fractals* 1996; **7**:293–301.
15. Keldermann RH, Nash MP, Panfilov AV. Pacemakers in a reaction–diffusion mechanics system. *Journal of Statistical Physics* 2007; **128**:375–392.
16. Nash MP, Panfilov AV. Electromechanical model of excitable tissue to study reentrant cardiac arrhythmias. *Progress in Biophysics and Molecular Biology* 2004; **85**:501–522.
17. Panfilov AV, Keldermann RH, Nash MP. Drift and breakup of spiral waves in reaction–diffusion–mechanics systems. *Proceedings of the National Academy of Sciences* 2007; **104**:7922–7926.
18. ten Tusscher KHWJ, Panfilov AV. Modelling of the ventricular conduction system. *Progress in Biophysics and Molecular Biology* 2008; **96**:152–170.
19. Rogers JM, McCulloch AD. A collocation–Galerkin finite element model of cardiac action potential propagation. *IEEE Transactions on Biomedical Engineering* 1994; **41**:743–757.
20. Rogers JM. Wave front fragmentation due to ventricular geometry in a model of the rabbit heart. *Chaos* 2002; **12**:779–787.
21. Göktepe S, Kuhl E. Finite element modeling of cardiac electrophysiology. *International Journal for Numerical Methods in Engineering* 2009; DOI: 10.1002/nme.2571.
22. Göktepe S, Wong J, Kuhl E. Atrial and ventricular fibrillation—Computational simulation of spiral waves in cardiac tissue. *Archive of Applied Mechanics*, submitted for publication, 2009.
23. Geselowitz D. On the theory of the electrocardiogram. *Proceedings of the IEEE* 1989; **77**:857–876.
24. Gulrajani RM. The forward and inverse problems of electrocardiography. *IEEE Engineering in Medicine and Biology* 1998; **17**:84–101.
25. Dubin D. *Rapid Interpretation of EKGs*. Cover Publishing Co: Fort Myers, 2000.
26. Ganong WF. *Review of Medical Physiology*. McGraw-Hill, Appleton & Lange: New York, 2003.
27. Durrer D, van Dam T, Freud E, Janse MJ, Meijlers FL, Arzbacher RC. Total excitation of the isolated heart. *Circulation* 1970; **41**:899–912.
28. Klabunde RE. *Cardiovascular Physiology Concepts*. Lippincott Williams & Wilkins: Philadelphia, 2005.